ARTICLES
PUBLISHED ONLINE: 12 DECEMBER 2010 | DOI: 10.1038/NPHYS1846
nature physics

A 1.8-THz quantum cascade laser operating significantly above the temperature of $\hbar\omega/k_B$

Sushil Kumar[1]*†, Chun Wang I. Chan[1], Qing Hu[1] and John L. Reno[2]

Several competing technologies continue to advance the field of terahertz science; of particular importance has been the development of a terahertz semiconductor quantum cascade laser (QCL), which is arguably the only solid-state terahertz source with average optical power levels of much greater than a milliwatt. Terahertz QCLs are required to be cryogenically cooled and improvement of their temperature performance is the single most important research goal in the field. Thus far, their maximum operating temperature has been empirically limited to $\sim\hbar\omega/k_B$, a largely inexplicable trend that has bred speculation that a room-temperature terahertz QCL may not be possible in materials used at present. Here, we argue that this behaviour is an indirect consequence of the resonant-tunnelling injection mechanism employed in all previously reported terahertz QCLs. We demonstrate a new scattering-assisted injection scheme to surpass this limit for a 1.8-THz QCL that operates up to $\sim 1.9\hbar\omega/k_B$ (163 K). Peak optical power in excess of 2 mW was detected from the laser at 155 K. This development should make QCL technology attractive for applications below 2 THz, and initiate new design strategies for realizing a room-temperature terahertz semiconductor laser.

The terahertz region of the electromagnetic spectrum ($\nu \sim 0.5$–10 THz, $\hbar\omega \sim 2$–40 meV, $\lambda \sim 600$–$30\,\mu$m) offers numerous applications in spectroscopy, remote-sensing and imaging[1,2]. Many molecules and solids have strong and distinct spectral signatures at terahertz frequencies, which makes terahertz technology important for both science and commercial applications. Some potentially important applications include remote-sensing of outer space and Earth's atmosphere, environmental monitoring, security-based imaging of concealed weapons, explosives or drugs, and biological and medical imaging. Although there has been a significant advancement in the field of terahertz science and technology[3,4], a commercially viable technique to generate narrowband and high-power terahertz radiation is lacking. Many of the above applications will benefit from compact continuous-wave sources of coherent terahertz radiation that will enable large signal-to-noise ratios for real-time imaging, and the use of large-array detectors for remote-sensing. Terahertz QCLs (ref. 5) are high-power, compact, solid-state continuous-wave sources of terahertz radiation that have witnessed rapid development in the past few years[6,7], and they are emerging as a viable technology with recent demonstrations of efficient techniques for continuous tunability[8] and low-divergence emission[9] of single-mode radiation. However, these devices require cryogenic cooling and their temperature performance worsens for designs at lower frequencies. The maximum reported operating temperature is 186 K for a 3.9 THz laser[10], which reduces to 69 K for a 1.2 THz laser[11]. Here, we report a new scattering-assisted injection design scheme for achieving high-temperature operation even for low-frequency ($\nu < 2$ THz) QCLs. The low-frequency emission shows negligible performance deterioration with increasing temperatures up to $\sim$110 K, which suggests that employing such a scheme may improve the maximum operating temperatures of high-frequency terahertz QCLs as well. The specific design presented here also realizes electrically switchable dual-frequency lasing as a by-product of its specific design scheme, and operates at 4 THz in the low-bias range up to 151 K temperature.

The resonant-tunnelling injection scheme in QCLs

Optical gain due to intersubband transitions in semiconductor superlattices was first investigated in 1971 (ref. 12). However, the original proposal required the device to be inherently operated in a negative-differential resistance (NDR) bias regime, which is electrically unstable owing to the formation of high-field domains in the superlattice[13]. The usage of an injector region in the semiconductor superlattice enabled it to maintain stable electrical bias in operation and was an important feature of the first demonstration of a mid-infrared intersubband (quantum cascade) laser[14]. The injector region has also remained a common feature of terahertz QCLs across different designs[5,15,16]. The performance of terahertz QCLs is particularly sensitive to the injector design owing to the small subband separations that make it difficult to selectively inject carriers (electrons) into the upper laser subband. Numerous terahertz QCL designs exist in the literature, but all of those share in common the resonant-tunnelling injection technique to populate the upper laser subband, and a maximum operating temperature (T_{max}) that is empirically no higher than $\sim\hbar\omega/k_B$ across all operating frequencies, as is shown in Fig. 1a. This behaviour can be qualitatively understood from an illustrative band diagram for the resonant-tunnelling injection mechanism shown in Fig. 1b. At low frequencies, the laser-level separation E_{ul} ($\sim$8 meV for $\nu \sim 2$ THz) becomes similar to the typical energy broadening of the subbands (a few millielectronvolts). Hence, it becomes difficult to selectively inject from $i \rightarrow u$, where i is the injector subband and u is the upper laser subband. The injector barrier is typically kept thick for low-frequency designs to keep the

[1]Department of Electrical Engineering and Computer Science and Research Laboratory of Electronics, Massachusetts Institute of Technology, Cambridge, Massachusetts, 02139, USA, [2]Sandia National Laboratories, Center of Integrated Nanotechnologies, Albuquerque, New Mexico, 87185, USA. †Present address: Department of Electrical and Computer Engineering and Center for Optical Technologies, Lehigh University, Bethlehem, Pennsylvania, 18015, USA. *e-mail: sushil@alum.mit.edu.

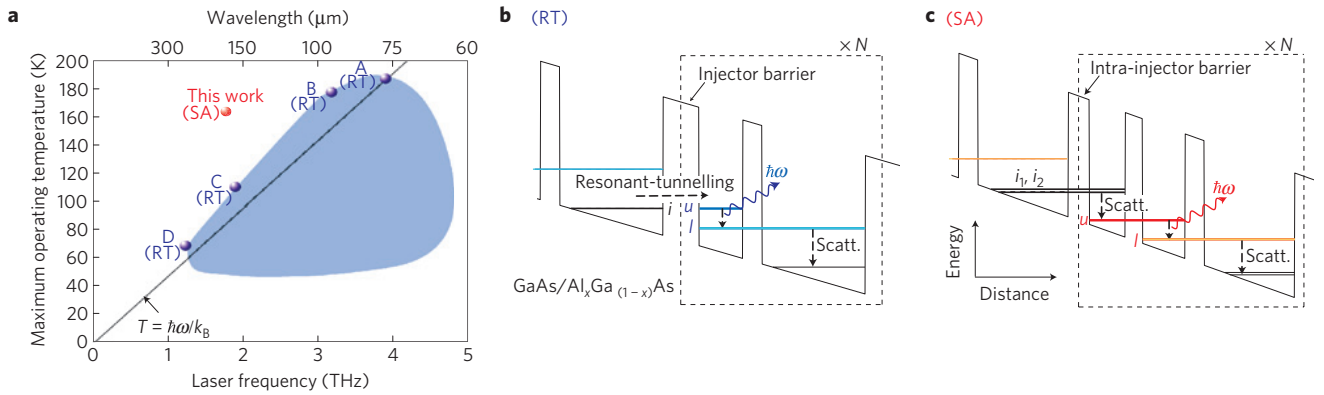

Figure 1 | Resonant-tunnelling versus scattering-assisted injection for terahertz quantum cascade lasers. a, Maximum operating temperature (T_{max}) versus frequency survey chart for terahertz QCLs (which operate without the assistance of a magnetic field), where the shaded area corresponds to a variety of reported designs[6]. The best reported terahertz QCLs in terms of T_{max} at selected frequencies are indicated by A, B, C, D corresponding to refs 10,32,17,11, respectively. All of the previously reported terahertz QCLs employ a resonant-tunnelling injection scheme, in contrast to the scattering-assisted injection scheme demonstrated in the present work. RT: resonant tunnelling; SA: scattering assisted. **b**,**c**, Illustrative band diagrams for the resonant-tunnelling (**b**) and scattering-assisted (**c**) injection schemes, where the radiative transition is from subband $u \rightarrow l$, and i, i_n is for the injector subband(s).

injection anticrossing splitting $2\hbar\Omega_{iu} \ll E_{ul}$ for superior injection selectivity and also to limit $i \rightarrow l$ leakage current. For example, injection anticrossings $2\hbar\Omega_{iu}$ for all such reported designs[17,18,11] are some of the smallest (<1 meV), which, however, makes the injector transport incoherent and inefficient[19,20]. Consequently, the dynamic range in current for the laser is reduced, which then limits the maximum operating temperature. See Supplementary Sections S1 and S2 for a more-detailed discussion of these aspects of resonant-tunnelling transport.

Advantages of a scattering-assisted injection scheme

Here, we show that the aforementioned problem with resonant-tunnelling injection could be circumvented by using a unique scattering-assisted injection mechanism, as illustrated in Fig. 1c. In this case, the cascade structure is designed to maximize current flow at a bias much higher than that for the i–u alignment. Consequently, potential barriers that typically limit the current flow owing to incoherent tunnelling (in this case, the intra-injector barrier as indicated in Fig. 1c) can be kept thinner to allow the resonant-tunnelling process to be coherent, even for a low-frequency design. The current transport now becomes a stronger function of overlap of the electron wavefunctions and their scattering cross-sections (primarily through longitudinal-optical (LO) phonons), rather than being limited by resonant tunnelling. Hence, the advantages of a scattering-assisted injection design scheme are twofold, both of which assist in obtaining a better temperature performance. First, it affords a greater dynamic range of operation for low-frequency terahertz QCLs by virtue of the specific injection scheme. In particular, whereas resonant-tunnelling injection allows only a small range of bias (that is, beyond the i–l alignment bias) in which selective injection is achieved into the upper subband u, the selectivity of injection for the scattering-assisted injection scheme is achieved when the $u \rightarrow l$ transition becomes diagonal. Such a condition is independent from the resonant-tunnelling transport through the current-limiting intra-injector barrier, which therefore allows a greater bias range to realize population inversion. Second, scattering-assisted injection allows the potential barriers to be kept thin, thereby allowing coherent resonant-tunnelling transport through the cascade structure. This weakens the sensitivity of the current injection to dephasing scattering processes, which are believed to become stronger with temperature and lead to a reduction in the peak gain[21]. Supplementary Sections S2 and S3 provide further details about the physical mechanisms that lead to the above-mentioned behaviour.

$k_B T_{max} \propto \hbar\omega$ behaviour of terahertz QCLs

Whereas the absolute $k_B T_{max} \sim \hbar\omega$ dependence for previously reported terahertz QCLs is coincidental (and therefore may lead to incorrect conclusions), the linear dependence of T_{max} with $\hbar\omega$ for terahertz QCLs with resonant-tunnelling injection can be understood from Fig. 2. The figure shows a numerical computation[22] of the population inversion $\Delta n_{ul} \equiv n_u - n_l$ (which is proportional to the peak intersubband gain) for one of the simplest representative terahertz QCL designs with such an injection scheme[23]. The primary observation from the results in Fig. 2b,c is the fact that the range of bias before the onset of NDR with positive gain (and consequently the dynamic range in current) reduces approximately linearly with the radiative energy separation E_{ul}. This behaviour can be understood from the following argument. In operating conditions, most of the carrier population resides in the injector subband. As the electrical bias is increased, the injector i first aligns with the lower radiative subband l, and then subsequently at a higher bias, aligns with the upper subband u. A population inversion between u and l is established only once the structure is biased past the i–l alignment, because then the electrons tunnel into the upper subband u preferentially (provided the NDR regime can be avoided until after the i–u alignment; see Supplementary Section S1 for further details). The operating bias range, which is up to the i–u alignment bias beyond which the NDR occurs, diminishes as E_{ul} becomes smaller, thereby reducing the dynamic range in lasing for current. Furthermore, $i \rightarrow l$ carrier leakage in the operating bias conditions (that is, close to the i–u alignment bias) is stronger for a low-frequency design, which further reduces the gain at lower frequencies, as is evident from smaller values of Δn_{ul}. Hence, even though low-frequency designs are more tolerant to thermally activated $u \rightarrow l$ LO-phonon scattering, which is one of the primary deterrents to high-temperature operation[6], T_{max} still monotonically decreases at lower frequencies. These arguments can qualitatively explain the observed $k_B T_{max} \sim \hbar\omega$ dependence for previously reported terahertz QCLs.

1.8-THz QCL based on scattering-assisted injection

The idea of scattering-assisted injection in QCLs is not new. Mid-infrared QCLs with a radiative transition directly from the

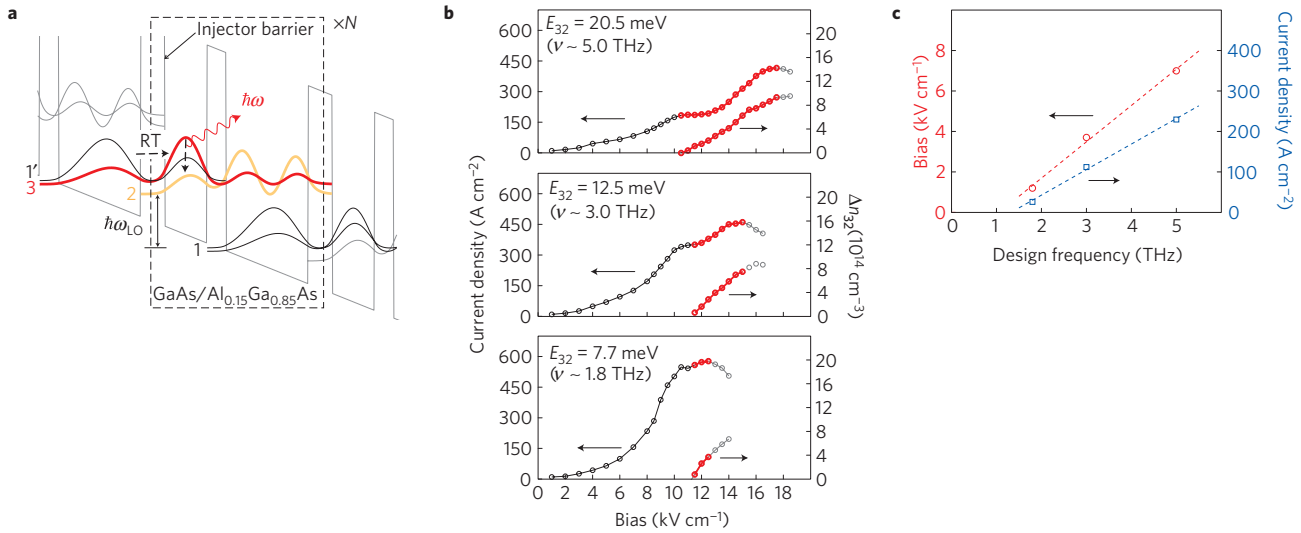

Figure 2 | Reduction in the operating dynamic range with frequency for resonant-tunnelling injection. a, Conduction band diagram at optimum injection bias (which occurs at 1′–3 resonance) for a two-well, three-level representative terahertz QCL design with resonant-tunnelling injection. The radiative transition is from 3 → 2, E_{21} is resonant with the LO-phonon energy ($\hbar\omega_{LO} \sim 36$ meV in GaAs) to enable fast depopulation of subband 2, and 1 is the injector subband. **b**, Numerically computed current density, and population inversion Δn_{32} (which is directly proportional to the peak gain), as a function of externally applied electrical bias field calculated for a lattice temperature of 25 K. The results were computed using an ensemble Monte Carlo simulation that accounted for the intramodule scattering mechanisms semiclassically and treated resonant-tunnelling transport within a density-matrix formalism with a phenomenological dephasing time $T_2^* = 0.33$ ps (ref. 22). Calculations are shown for three different frequency designs, keeping other important design parameters the same (injection anticrossing $2\hbar\Omega_{1'3} \sim 1.5$ meV, radiative oscillator strength $f_{32} \sim 0.6$, and average doping 5×10^{15} cm^{-3}). Optimum injection (that is, the bias for the maximum of the current density) occurs at the 1′–3 alignment bias field that decreases with E_{32} thereby decreasing the bias range in which gain is positive. The curves are highlighted in red (thick lines) for the 'usable' bias region in which the gain is positive before the occurrence of NDR. **c**, The dynamic range for positive population inversion before the occurrence of the NDR is extracted from the numerical results of **b**. A linear reduction of both the voltage and the current dynamic ranges with the designed frequency is apparent.

lowest subband of the injector miniband were reported early[24,25]. QCLs with various indirect injection schemes from the injector minibands have also been realized[26–28]. However, the design considerations and transport characteristics of mid-infrared QCLs are markedly different from those of terahertz QCLs owing to the much larger radiative energy separation in the former. Selective injection and depopulation of carriers is much more difficult to achieve at terahertz frequencies. A scattering-assisted injection scheme may therefore promise unique advantages for terahertz QCLs. Recently, a five-well terahertz QCL design consisting of four injector subbands was proposed and studied theoretically[29]. At low temperatures, high gain was predicted in that particular design owing to a greater carrier accumulation in the upper radiative subband; however, the calculated gain diminished rapidly at higher temperatures owing to a thermally activated LO-phonon scattering process. A wide variety of designs with scattering-assisted injection are possible; the present report is the first experimental demonstration of a terahertz QCL with such an injection scheme, in which we have shown a much improved temperature performance for low-frequency operation that is attributed to an improvement in the selectivity of injection into the upper radiative subband, and also to a lower sensitivity of the electron transport to dephasing scattering.

The specific design in this Article uses two injector subbands (labelled 1 and 2) and is shown in Fig. 3a. A minimum of two injector subbands are necessary for a scattering-assisted injection design scheme. This is because the 'operating-bias' condition, which corresponds to that of maximum current flow across the structure before the occurrence of the NDR, is required to occur much beyond the i_n–u alignment for such a design. The current transport could be guaranteed to increase up until the operating bias by implementing multiple injector subbands that get energetically aligned at resonance only at the desired bias condition (for example, the i_1–i_2 resonance in Fig. 1c). In contrast, the operating bias for designs based on resonant-tunnelling injection is determined by the injector upper subband resonance (that is, the i–u resonance in Fig. 1b), in which case designs with a single injector subband are possible[17]. In Fig. 3a, the scattering-assisted injection occurs from $(2', 1') \rightarrow 5$ and the desired radiative transition is from $5 \rightarrow 4$. Depopulation of lower radiative subband 4 occurs through the resonant-phonon scheme similar to that of ref. 15. For optimum injection at low temperatures, $E_{1'5}$ should be kept resonant with $\hbar\omega_{LO}$ (~36 meV in GaAs) for efficient electron–LO-phonon scattering; however, in our implementation, $E_{1'5}$ is kept smaller (~20 meV) for two reasons. First, larger $E_{1'5}$ requires taller potential barriers, which makes all of the barriers thinner in the design and might affect the temperature performance owing to the larger effect of interface roughness on transport. Second, larger $E_{1'5}$ brings the injector subbands 1′ and 2′ closer in energy to higher-energy subbands in the quantum wells, which may degrade the temperature performance of the laser owing to parasitic thermal leakage of carriers[23]. As the present design is aimed at high-temperature operations, thermally activated electron–LO-phonon scattering is readily available even though $E_{1'5} < \hbar\omega_{LO}$.

Experimental results

Figure 3b shows a numerical computation for the designed quantum cascade structure. Positive population inversion is realized for the desired $5 \rightarrow 4$ transition at 1.8-THz with a greater dynamic range in bias and current than that achievable by the resonant-tunnelling injection scheme of Fig. 2 for comparable design parameters. The cascade structure was grown, processed into metal–metal ridge cavities and experimentally characterized using standard techniques[10]. Figure 3c shows low-temperature (10 K) electrical and optical characteristics in pulsed operation

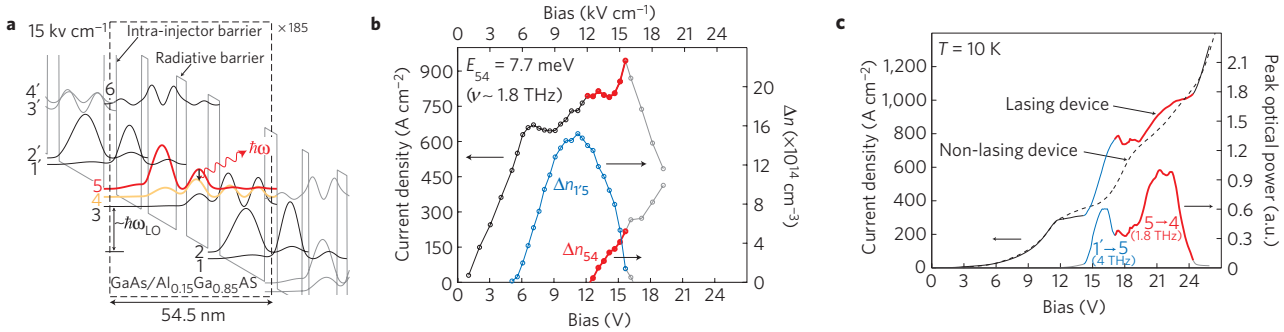

Figure 3 | A 1.8-THz QCL based on the scattering-assisted injection design scheme. a, Conduction band diagram at optimum injection bias of a four-well design with scattering-assisted injection and resonant-phonon depopulation for a 1.8-THz radiative transition from 5 → 4 ($E_{54} \sim 7.7$ meV as calculated). Also, the anticrossing $2\hbar\Omega_{12} \sim 3$ meV, radiative oscillator strength $f_{54} \sim 0.6$ at the shown bias, and average doping in the structure is 5.7×10^{15} cm^{-3}. **b**, Numerical computation (similar to Fig. 2b) of current density and population inversion as a function of externally applied electrical bias for a lattice temperature of 25 K. The regions of positive gain for the 5 → 4 transition before the occurrence of NDR are highlighted in red (thick lines). A population inversion for the 1′–5 transition is also established in this design scheme and is plotted in blue. **c**, Low-temperature current–voltage (I–V) and light–voltage (L–V) characteristics from a 0.8 mm × 80 μm × 10.1 μm metal–metal ridge cavity laser. The red region corresponds to 1.8-THz emission due to the 5 → 4 transition with scattering-assisted injection. The device also achieves lasing at 4 THz at low bias due to the aforementioned 1′ → 5 transition, which is indicated in blue. The dashed curve shows the I–V characteristic of the same device from a control measurement when its lasing was suppressed by surrounding the cavity with an insulating layer of an epoxy resin (Stycast 2850FT). The increased current flow below a bias of 18 V for the lasing device is due to the 1′ → 5 stimulated emission[20], which also leads to an occurrence of an NDR feature at 18 V when the 1′ → 5 lasing action ceases.

from a representative device, which lased predominantly at 1.8-THz as highlighted in red. Lasing ceases at a bias of ~24 V triggered by a steep increase in current in the current–voltage (I–V) characteristic. This is probably due to electrons tunnelling from injector subbands into the continuum of states above the potential barriers owing to the relatively high bias field in that condition. Note that this aspect of electron transport is not modelled in the numerical computation of Fig. 3b, which, instead, predicts a sharp drop in current beyond a certain bias (~16 V). As a by-product of keeping $E_{1'5} < \hbar\omega_{LO}$ (that is, off-resonant to the Reststrahlen band absorption of the semiconductor) and the fact that the 1′ → 5 transition also develops population inversion as shown in Fig. 3b, the device also realizes lasing action at ~4 THz at lower bias, which is indicated in blue in Fig. 3c. Four-well terahertz QCLs similar to the present design have been reported previously[30,31] but designed specifically for the 1′ → 5 radiative transition that uses resonant-tunnelling injection. However, the present design has an important difference in that subbands 1 and 2 are strongly coupled ($2\hbar\Omega_{12} \sim 3.0$ meV as compared with ~1.9 meV in ref. 30 and 1.0 meV in ref. 31) such that they form a doublet of injector levels and the transport is limited by their lifetime rather than the thickness of the injector barrier[20]. Another important difference is that the radiative barrier, as labelled in Fig. 3a, is kept significantly thinner to allow coherent radiative transport for the 5 → 4 transition.

The experimental I–V curve in Fig. 3c shows a mild NDR once 1′ → 5 lasing stops at a bias voltage of ~18 V. We believe that this happens because the increased current flow due to 1′ → 5 stimulated emission[20] ceases with the 1′ → 5 lasing action. In Fig. 3c, the optical power due to 1′ → 5 emission is at a decline before the occurrence of the NDR feature at 18 V. This suggests that the extra current flow due to stimulated emission is also at a decline with bias, which eventually leads to a negative slope in the I–V of the lasing device, thus causing an NDR. Further experimental evidence of this behaviour is provided in Supplementary Section S4. A control measurement of the device when its optical characteristics were altered to suppress lasing without affecting its electrical transport behaviour did not show the NDR feature at 18 V, as shown in Fig. 3c, giving further support to this hypothesis. Whereas the I–V characteristics of the lasing versus non-lasing devices differ at low temperatures (as shown in Fig. 3c), at high temperatures (>165 K), the I–Vs in both cases were the same (not shown). This suggests that the use of an insulating epoxy encapsulant to suppress lasing did not alter the device's electrical behaviour. The exact mechanism of lasing suppression was not investigated, but it is probably a combination of the fact that epoxy is optically lossy and also worsens the mode confinement of the waveguide. We note that the above speculation is not definitive evidence of the cause of the NDR feature; an electrical transport contribution due to misalignment of subbands 1′ and 2′ as in conventional devices with resonant-tunnelling injection should not be discounted as another possible cause for the discontinuity in the I–V.

The optical emission from the QCL is maximum at a bias of ~21 V, which is considerably higher than the optimum injection bias of ~16 V as predicted in simulation (Fig. 3b). An extra 3–4 V voltage drop at the metal–semiconductor Schottky electrical contact is typical of terahertz QCLs, as has been observed in refs 18,10. An even higher operating voltage in this QCL is probably due to some inhomogeneous electrical biasing across different QCL modules triggered by the aforementioned NDR feature at 18 V. Finally, it may be noted that the 5 → 4 emission at 1.8-THz starts before the occurrence of the NDR feature when the 1′ → 5 emission at 4 THz is still active, which leads to simultaneous occurrence of dual-frequency emission in a narrow bias range close to that bias. However, the 4 THz emission ceases beyond the NDR feature at 18 V, when the 1.8-THz emission becomes stronger. The two types of emission therefore occur in an almost mutually exclusive bias regime. This behaviour is explained as follows. At low bias, subband 5 is in anticrossing with subbands 4 and 3, and hence is efficiently depopulated, leading to the 4-THz 1′ → 5 inversion ($\Delta n_{1'5} > 0$). With increasing bias, 5 and 4 are no longer in resonance and electrons accumulate in subband 5, which diminishes $\Delta n_{1'5}$ and enhances Δn_{54}. The spectral behaviour of the laser as a function of bias is reported in greater detail in Supplementary Section S4.

Robust temperature performance at $\nu \sim 1.8$-THz

A primary feature of the design presented here is the robust temperature performance of the 5 → 4 radiative transition at 1.8-THz, which features the new scattering-assisted injection scheme. The

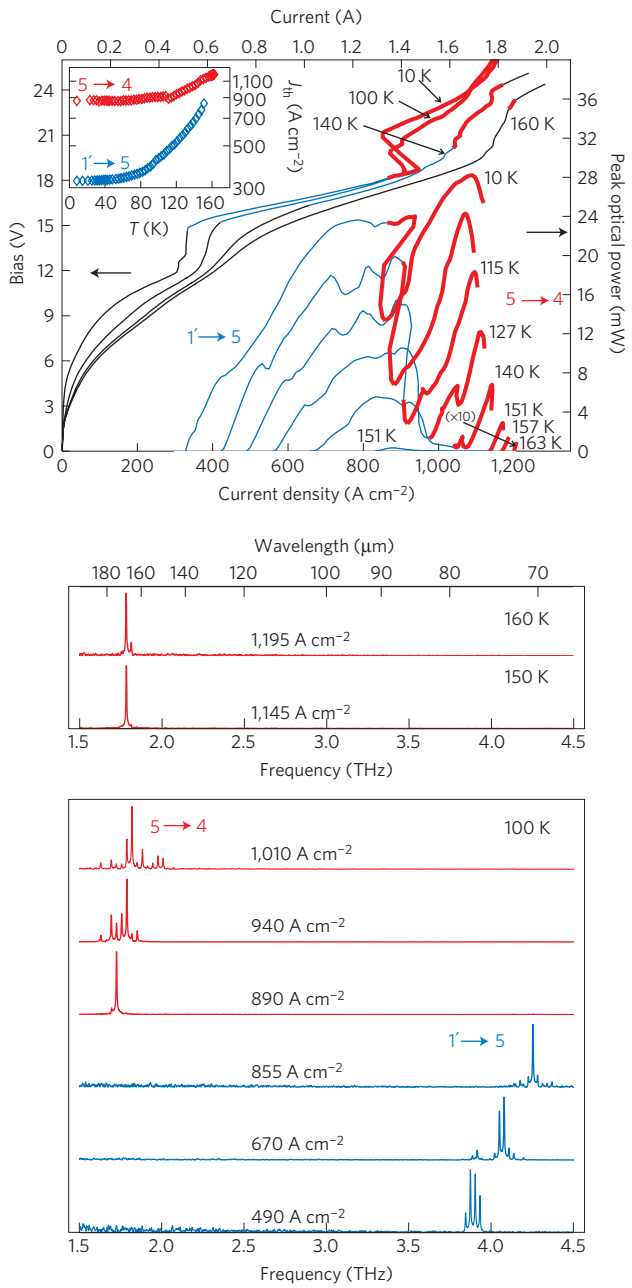

Figure 4 | Experimental results as a function of temperature. **a**, Current–voltage (*I*–*V*) and light–current (*L*–*I*) characteristics from an edge-emitting 1.3 mm × 120 μm × 10.1 μm metal–metal ridge cavity laser as a function of the heat-sink temperature. The reported power is as detected by the power meter from a single facet of the cavity without any corrections. Emission at 1.8-THz (5 → 4 transition) and 4 THz (1′ → 5 transition) is highlighted in red and blue, respectively. At low temperatures (≲100 K), the 1.8-THz emission starts before the occurrence of an NDR feature in the *I*–*V*s at ∼18 V, which leads to simultaneous dual-frequency emission in a narrow bias range (detailed spectra and *L*–*I* that highlight this aspect of the laser are shown in Supplementary Section S4). Inset: Variation of the threshold current density J_{th} with temperature T, with values of $J_{th,10\,K} \sim 865$ A cm^{-2} and $J_{th,10\,K} \sim 325$ A cm^{-2} for the two transitions, respectively. **b**, Normalized intensity spectra at different bias and temperatures for the same device and plotted on a linear vertical scale.

temperature behaviour of the *I*–*V* and *L*–*I* characteristics as well as lasing spectra for a wider ridge laser are plotted in Fig. 4. Lasing action at 1.8-THz is observed up to a temperature of 163 K (that is, $k_B T_{max} \sim 1.9\,\hbar\omega$, an unprecedented result for any solid-state laser that operates without the assistance of an external magnetic field). The observed threshold current density J_{th} for the 1.8-THz emission, as plotted in the inset of Fig. 4a in red, remains independent of the heat-sink temperature T approximately up to 110 K, which is arguably a significantly higher turn-on temperature than that for any of the previously reported terahertz QCLs. The weak temperature dependence of J_{th} with temperature is attributed to decreased sensitivity of the injection process to dephasing scattering. This is because the resonant-tunnelling transport across the current-limiting potential barrier (that is, the intra-injector barrier in this design) can be kept coherent, as described previously. Although it is difficult to verify the above speculation experimentally, arguments based on numerical and analytical modelling of resonant-tunnelling transport are provided in Supplementary Sections S2 and S3, respectively, to support this hypothesis. From Fig. 4a, it is important to note that the device showed a better temperature performance for the 1.8-THz transition than that for the 4 THz transition ($T_{max} \sim 151$ K), despite the fact that the 4 THz transition from 1′ → 5 showed a larger gain in the numerically computed results at $T = 25$ K, as shown in Fig. 3b. The computations were repeated for a temperature of 200 K (not shown), which still showed positive population inversion for both the transitions, with the 4 THz (1′ → 5) transition showing a larger gain contrary to the experimental observations. It is then likely that thermal leakage from 1′, 2′ to high-energy quasi-bound parasitic subbands in the adjacent quantum wells[23], which is not accounted for in the numerical code of ref. 22, reduces the 1′ → 5 gain more rapidly with temperature as compared with gain due to the 5 → 4 radiative transition. The experimental behaviour of this QCL clearly demonstrates that more sophisticated theoretical models are needed to accurately describe the temperature behaviour of terahertz QCLs.

We have presented a new scattering-assisted injection design scheme for terahertz QCLs, which is shown to significantly improve the temperature performance of low-frequency ($\nu < 2$ THz) QCLs. This is attained because the selectivity of the injection process into the upper radiative subband in such a design is no longer restricted by the bias dependence of the dominant resonant-tunnelling current transport in the quantum cascade structure. Furthermore, it is argued that such a scheme affords a design with coherent resonant-tunnelling transport across the current-limiting potential barriers. This makes electrical transport less sensitive to dephasing scattering, which is known to become stronger with temperature. Experimentally, a 1.8-THz QCL operating up to a heat-sink temperature of 163 K ($\sim 1.9\,\hbar\omega/k_B$) is realized, which is significantly greater than the empirical temperature limit of $\sim\hbar\omega/k_B$ observed for previously reported terahertz QCLs that have used resonant tunnelling for injection into the upper radiative subband. The threshold current density for the demonstrated laser remains approximately independent of temperature up to ∼110 K, which is the highest such turn-on temperature observed experimentally for terahertz QCLs, attesting to a lower sensitivity to temperature degradation mechanisms in this design. Subsequent improvements to the design, such as making the radiative transition more diagonal[10], are likely to improve the maximum operating temperatures for terahertz QCLs even further.

Methods

The structure, labelled OWI185E-M1 (wafer VB0244), was grown by molecular beam epitaxy with 185 cascaded periods, with $n = 5 \times 10^{18}$ cm^{-3} contact layers grown above (50 nm thick) and below (100 nm thick) the 10.1-μm-thick active region, and with a 200 nm $Al_{0.55}Ga_{0.45}As$ etch-stop layer underlying the entire epitaxially grown region. In Fig. 3a, starting from the injector barrier, the layer thicknesses in nanometres are **4.2**/8.5/**2.3**/9.6/**3.4**/7.3/**4.0**/15.3, with the barriers indicated in bold font. The widest well was n-doped to 2.05×10^{16} cm^{-3}, yielding an average doping of 5.7×10^{15} cm^{-3} per QCL period.

Metal–metal waveguide ridge lasers were processed by wet-etching using the method outlined in ref. 10 with a Ta/Cu/Ti/Au layer sequence for the top metal and Ta/Cu for the bottom metal of the finally processed ridge waveguides. The fabricated devices were cleaved (with back facets left uncoated), indium-soldered ridge side up on a copper mount, wire bonded, and mounted on the cold stage of a pulsed-tube cryocooler for measurements.

Optical power was detected from a single facet when collected with a Winston cone (with a circular opening of 1.9 mm diameter) and the detector was placed adjacent to the cryostat window. Device spectra were measured at a resolution of 3.75 GHz in linear scan mode with a Nicolet Magna 850 infrared spectrometer that was purged with nitrogen gas to limit any atmospheric water absorption. The device was operated in pulsed mode with 300 ns pulses repeated at 300 Hz, and power was detected using a He-cooled broadband Si bolometer that had a diamond absorber and a 5 THz high-frequency cutoff filter, for both the *L–I* and the spectral measurements. To get an accurate estimate of the threshold current density of the 1.8-THz emission in Fig. 4a, the J_{th} versus T data were extracted from a repeat measurement of the *L–I* with an InSb hot-electron bolometer that had an intrinsic high-frequency roll-off above 1.5 THz leading to negligible detection of the 4 THz radiation. Absolute power measurements were carried out separately with a calibrated thermopile power meter (ScienTech, model AC2500) placed adjacent to the cryostat window, at a duty cycle of 10% (1 μs pulses repeated at 100 kHz). The power detected by the power meter is reported without any corrections.

Received 11 March 2010; accepted 11 October 2010; published online 12 December 2010

References

1. Siegel, P. H. Terahertz technology. *IEEE Trans. Microwave Theory Tech.* **50,** 910–928 (2002).
2. Chan, W. L., Diebel, J. & Mittleman, D. M. Imaging with terahertz radiation. *Rep. Prog. Phys.* **70,** 1325–1379 (2007).
3. Ferguson, B. & Zhang, X-C. Materials for terahertz science and technology. *Nature Mater.* **1,** 26–33 (2006).
4. Tonouchi, M. Cutting-edge terahertz technology. *Nature Photon.* **1,** 97–105 (2007).
5. Köhler, R. *et al.* Terahertz semiconductor-heterostructure laser. *Nature* **417,** 156–159 (2002).
6. Williams, B. S. Terahertz quantum-cascade lasers. *Nature Photon.* **1,** 517–525 (2007).
7. Scalari, G. *et al.* THz and sub-THz quantum cascade lasers. *Laser Photon. Rev.* **3,** 45–66 (2009).
8. Qin, Q., Williams, B. S., Kumar, S., Hu, Q. & Reno, J. L. Tuning a terahertz wire laser. *Nature Photon.* **3,** 732–737 (2009).
9. Amanti, M. I., Fischer, M., Scalari, G., Beck, M. & Faist, J. Low-divergence single-mode terahertz quantum cascade laser. *Nature Photon.* **3,** 586–590 (2009).
10. Kumar, S., Hu, Q. & Reno, J. L. 186 K operation of terahertz quantum-cascade lasers based on a diagonal design. *Appl. Phys. Lett.* **94,** 131105 (2009).
11. Walther, C. *et al.* Quantum cascade lasers operating from 1.2 to 1.6 THz. *Appl. Phys. Lett.* **91,** 131122 (2007).
12. Kazarinov, R. F. & Suris, R. A. Possibility of the amplification of electromagnetic waves in a semiconductor with a superlattice. *Sov. Phys. Semicond.* **5,** 707–709 (1971).
13. Bonilla, L. L. & Grahn, H. T. Non-linear dynamics of semiconductor superlattices. *Rep. Prog. Phys.* **68,** 577–683 (2005).
14. Faist, J. *et al.* Quantum cascade laser. *Science* **264,** 553–556 (1994).
15. Williams, B. S., Callebaut, H., Kumar, S., Hu, Q. & Reno, J. L. 3.4-THz quantum cascade laser based on longitudinal-optical-phonon scattering for depopulation. *Appl. Phys. Lett.* **82,** 1015–1017 (2003).
16. Scalari, G. *et al.* Far-infrared ($\lambda \cong 87\,\mu m$) bound-to-continuum quantum-cascade lasers operating up to 90 K. *Appl. Phys. Lett.* **82,** 3165–3167 (2003).
17. Kumar, S., Williams, B. S., Hu, Q. & Reno, J. L. 1.9 THz quantum-cascade lasers with one-well injector. *Appl. Phys. Lett.* **88,** 121123 (2006).
18. Walther, C., Scalari, G., Faist, J., Beere, H. & Ritchie, D. Low frequency terahertz quantum cascade laser operating from 1.6 to 1.8-THz. *Appl. Phys. Lett.* **89,** 231121 (2006).
19. Sirtori, C. *et al.* Resonant tunneling in quantum cascade lasers. *IEEE J. Quantum Electron.* **34,** 1722–1729 (1998).
20. Kumar, S. & Hu, Q. Coherence of resonant-tunneling transport in terahertz quantum-cascade lasers. *Phys. Rev. B* **80,** 245316 (2009).
21. Nelander, R. & Wacker, A. Temperature dependence of the gain profile for terahertz quantum cascade lasers. *Appl. Phys. Lett.* **92,** 081102 (2008).
22. Callebaut, H. & Hu, Q. Importance of coherence for electron transport in terahertz quantum cascade lasers. *J. Appl. Phys.* **98,** 104505 (2005).
23. Kumar, S., Chan, C. W. I., Hu, Q. & Reno, J. L. Two-well terahertz quantum-cascade laser with direct intrawell-phonon depopulation. *Appl. Phys. Lett.* **95,** 141110 (2009).
24. Faist, J. *et al.* Laser action by tuning the oscillator strength. *Nature* **387,** 777–782 (1997).
25. Gmachl, C. *et al.* Bidirectional semiconductor laser. *Science* **286,** 749–752 (1999).
26. Scamarcio, G. *et al.* High peak power (2.2 W) superlattice quantum cascade laser. *Electron. Lett.* **37,** 295–296 (2001).
27. Yamanishi, M., Fujita, K., Edamura, T. & Kan, H. Indirect pump scheme for quantum cascade lasers: Dynamics of electron-transport and very high T_0-values. *Opt. Express* **16,** 20748–20758 (2008).
28. Franz, K. J. *et al.* High k-space lasing in a dual-wavelength quantum cascade laser. *Nature Photon.* **3,** 50–54 (2009).
29. Yasuda, H. *et al.* Nonequilibrium green's function calculation for four-level scheme terahertz quantum cascade lasers. *Appl. Phys. Lett.* **94,** 151109 (2009).
30. Kumar, S., Hu, Q. & Reno, J. L. *Conference on Lasers and Electro-Optics*, OSA Technical Digest, paper CThH4, (2009), http://www.opticsinfobase.org/abstract.cfm?URI=CLEO-2009-CThH4.
31. Amanti, M. I. *et al.* Bound-to-continuum terahertz quantum cascade laser with a single-quantum-well phonon extraction/injection stage. *New J. Phys.* **11,** 125022 (2009).
32. Belkin, M. A. *et al.* Terahertz quantum cascade lasers with copper metal–metal waveguides operating up to 178 K. *Opt. Express* **16,** 3242–3248 (2008).

Acknowledgements

This work is supported by the National Aeronautics and Space Administration and the National Science Foundation. The work was carried out in part at the United States Department of Energy, Center for Integrated Nanotechnologies, and Sandia National Laboratories (Contract DE-AC04-94AL85000).

Author contributions

S.K. designed the quantum cascade structure in consultation with Q.H., processed the devices and did some initial experiments. C.W.I.C. carried out detailed experiments and characterization. S.K., C.W.I.C. and Q.H. analysed the experimental data. J.L.R. was responsible for the crystal growth by molecular beam epitaxy. S.K. wrote the manuscript with assistance from all other authors. The project was supervised by Q.H.

Additional information

The authors declare no competing financial interests. Supplementary information accompanies this paper on www.nature.com/naturephysics. Reprints and permissions information is available online at http://npg.nature.com/reprintsandpermissions. Correspondence and requests for materials should be addressed to S.K.